GAUGE FACTOR OF GRAPHENE PIEZORESISTOR FOR SURFACE ACOUSTIC WAVE GYROSCOPE INSTRUMENTATION

A Thesis

Presented to the Faculty of the Graduate School

of Cornell University

in Partial Fulfillment of the Requirements for the Degree of

Master of Science

by

Shrinidhi Srikanth Kulkarni

August 2018

ABSTRACT

Surface Acoustic Wave gyroscopes are gyroscopes that have no suspended structures and hence have the potential of operation under high shock and vibration environments. Typically, gyroscopes have two electro-mechanical resonators; a drive resonator which couples energy into the sense resonator through the Coriolis force. Challenges in SAW gyroscope instrumentation include the matching of drive and sense resonance frequencies, matching to 50 Ωimpedance for electronics, and maximizing sensitivity while minimizing noise. In addition the sensitivities to accelerations and other physical effects such as temperature swings need to be minimized. Piezoresistive graphene transducers, with high sensitivity, and ultra-low mass density and negligible loading of SAW waves, and matching to 50 Ωby proper sizing, can provide a pathway to improving SAW gyroscope performance.

In this thesis, we study the electrode design and the alignment of graphene piezoresistive transducers in a two port SAW resonator to maximize the sensitivity obtained by a biasing technique. By applying an external bias, current induced by SAW in graphene resistors can be canceled and large sensitivity at this bias point can be obtained. To characterize the sensitivity of graphene electrodes, we vary the widths, lengths and placement of the piezoresistor.

We calculate the effective gauge factor using the measured displacement as a function of RF amplitude. We have discovered that the piezoresistors of $\lambda/4$ width, aligned between the node and antinode of the primary SAW will be the most sensitive configuration equivalent to an effective gauge factor of 1×10^8. This high gauge factor, enabled by fast digital processing, can lead to highly

sensitive SAW gyroscopes and other electromechanical sensors.

BIOGRAPHICAL SKETCH

Shrinidhi Kulkarni was born in Bengaluru, India. He graduated from Sri Jayachamarajendra College of Engineering (Mysuru, India) with a Bachelor of Engineering degree in Electronics and Communication in 2016. He came to the United States soon after and joined the School of Applied & Engineering Physics at Cornell University for their Masters program.

Apart from academics, Shrinidhi is actively involved in several activities across the campus. He is the co-president of the India Association at Cornell and an event coordinator of the Applied Physics Graduate Society. He loves traveling and doing astro-photography.

After completing his Masters, he will be joining Western Digital as a Senior Systems Design Engineer, working on system design of solid state drives.

To my parents

ACKNOWLEDGEMENTS

I would like to offer my deepest gratitude to my advisor, Professor Amit Lal, for his guidance, support and patience with my work. His breadth of knowledge and enthusiasm into problems have always impressed me and inspired my research. I am very grateful for the freedom and financial support he has provided.

I would like to thank my committee member, Professor Christopher Ober for being patient and accommodating. I also thank Professor David Muller and Professor Joel Brock for their guidance in the AEP masters program. I thank the staff for their support - Cynthia Reynolds, Renee King and Nicole LaFave for their help and patience.

This work has largely been done as a part of the DARPA AIMS program. A special thanks to my team - Benyamin Davaji and Visarute (Earth) Pinrod - for guiding me throughout my time here and helping me with the experimental setups. Special thanks to Daniel Teal from UT Austin for the python script to automate the experiment.

I would also like to thank every member in SonicMEMS Lab especially Sachin Nadig, Adarsh Ravi and Ved Gund for their moral support, Vinaya Kumar for his insightful comments and ideas, Alexander Ruyack for getting me familiar with the ways of the group when I joined the group initially.

This section is incomplete without thanking my friends, especially Suhas Shrinivasan, Srinath Ranya, Surabhi Ramesh and Rakesh Sharma for putting strength in me during my time at Cornell. Last, but by no means least, I cannot express how deeply indebted I am to my family for their unwavering love, support and encouragement, without which none of this would have been possible.

TABLE OF CONTENTS

LIST OF TABLES

LIST OF FIGURES

CHAPTER 1

INTRODUCTION

Graphene is fundamentally a single layer of sp^2 bonded carbon atoms arranged in a hexagonal lattice structure. Structurally, it is similar to the commonly available graphite or 'pencil lead'. However, it offers impressive properties that are very different from its mother material. Graphite is essentially a 3-D stacked version of graphene and highly brittle, while Graphene is one of the strongest materials every recorded, more than forty times stronger than diamond. It can be considered as the fundamental building block for all forms of graphitic carbon (fullerenes, carbon nanotubes, graphite) as shown in Fig. 1.1.[1]

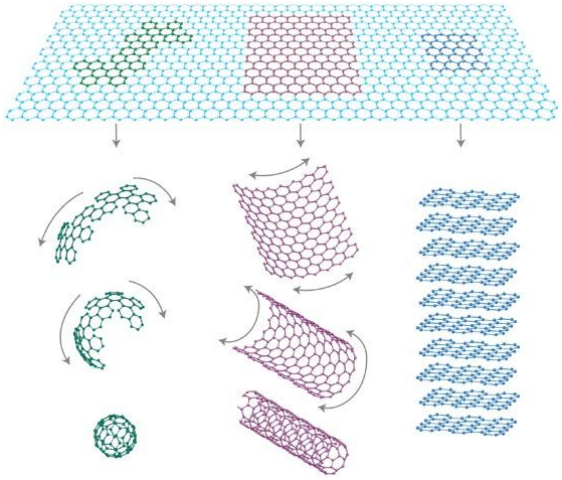

Figure 1.1: Graphene is a 2D building material for all other forms of graphitic carbon. Illustration from [1]

Though graphene had been extensively studied, single layer graphene remained undetected for several years until 2004, when A. Geim and K. Novoselov successfully isolated single graphene crystals using adhesive tape [2]. Over the last few decades, graphene research has grown at a great pace, with efforts being made to realize its potential is various applications, ranging from

optical electronics, as a replacement for Indium Tin Oxide to fuel cells, where graphene sheets are used to modulate electrochemical reaction in a controlled fashion. Graphene has also been used in chemiresistors in chemical sensors, and also in micro-electronics and nano-photonics.

The unique properties of graphene has led to a multitude of devices that rely on the interaction of graphene with surface acoustic waves (SAW) including humidity detectors, mass sensors, and photodetectors [3],[4],[5]. These devices rely on the interaction of graphene to measure physical changes in the SAW propagation speed, amplitude, or frequency, as detection methods.

This interaction also produces acoustoelectric (AE) current in the directions both parallel and transverse to wave propagation, as shown in Fig. 1.2 [6], that is commonly used to probe or modulate the electrical properties of the graphene.

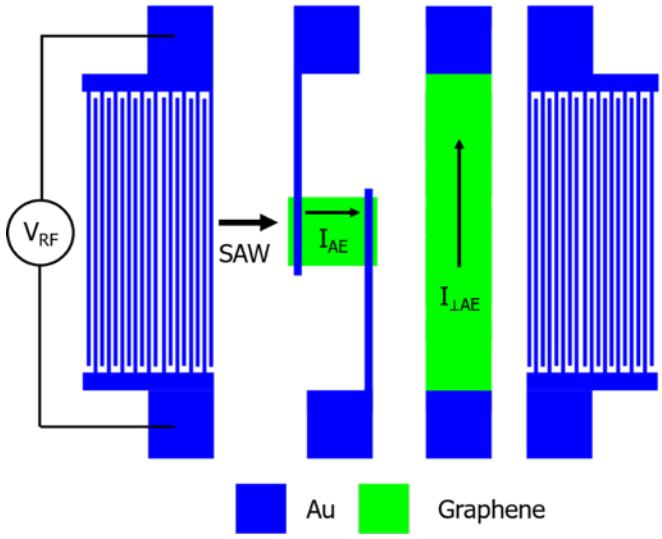

Figure 1.2: Acoustoelectric effect in graphene

The AE effect can be used as a sensing mechanism such as in probing the photo response of graphene [7], despite its ability to directly indicate the presence of SAWs. Several approaches have been used to use graphene as an elec-

trode material to avoid the mass loading associated with metal electrodes [8].

1.1 Motivation and Approach

Commonly, inter-digitated transducers(IDTs) are used for the detection and measurement of SAWs on piezoelectric substrates. Some of the most common piezoelectric substrates are quartz, Lithium Niobate ($LiNbO_3$) and GaAs. $LiNbO_3$ is usually used due to its high electromechanical coupling coefficient. For most cases, IDTs are preferably fabricated from inert metals such as gold or platinum.

However, in high frequency applications mass-loading effects restrict the usage of such materials: the inertia of the transducer fingers reduces the magnitude of the generated acoustic wave; the dense metal will also reflect the mechanical waves. To avoid such effects, high frequency IDTs are usually made from metals with a relatively low density such as Al/Ti, and are often embedded into the substrate to reduce undesirable reflections[9]. Another approach has been used at room temperature is to form IDTs from a two-dimensional electron system (2DES) in an AlGaN/GaN heterostructure, but this has a significant drawback since the insertion loss is greater than 80dB, mainly due to the resistive loss arising from the 2DES.[10] In some cases the reflection coefficient are used to construct resonators.

Graphene has recently become a promising choice for high frequency IDTs since it is conductive, whilst also being the thinnest and lightest material that can be easily processed by conventional photolithography.[2] As such, no significant mass loading is expected from IDTs made of graphene. [11] [4]

Strain gauges are commonly used transducers for electrical measurement of mechanical quantities. They are sensors that measure change in strain due to internal or external factors such as force, pressure, tension, etc. Usually, strain gauges work as sensors whose resistance changes as a function of the strain. A fundamental parameter of the strain gauge is its sensitivity to strain, expressed quantitatively as the gauge factor (GF). Gauge factor is defined as the ratio of fractional change in electrical resistance to the fractional change in length (strain):

$$GF = \frac{\Delta R/R}{\varepsilon} \tag{1.1}$$

Typically, gauge factor of metals is small (2-5). In practice, the strain measurements rarely involve quantities larger than a few millistrain ($\varepsilon \times 10^3$). Therefore, measurement of strain requires accurate measurement of tiny changes in resistance. For example, suppose a test specimen undergoes a substantial strain of $500\mu\varepsilon$. A strain gauge with a gauge factor GF = 2 will exhibit a change in electrical resistance of only $2 \cdot (500 \times 10^6) = 0.1\%$. For a 120 Ωgauge, this is a change of only 0.12 Ω.

In this work, we obtain a very high gauge factor of graphene which we believe can be the underlying principle of a new class of SAW transducers. Measurement of the output from SAW sensors usually requires RF signal conditioning circuits which are complex and have a high power consumption. With graphene, the measurement would be much simpler. DC measurements are relatively easy to perform as compared to high frequency AC measurements.

The goal of the work presented in this thesis is to enable simpler measurement from SAW gyroscopes. The basics of gyroscopes, overview and analysis of SAW, and the principle of SAW gyroscopes is presented Chapter 2. Chapter

3 explains the design considerations and the experimental setup. In Chapter 4, we illustrate and discuss the results of the experiments. A summary is given in Chapter 5, together with possible pathways for improved results as future work.

CHAPTER 2

SAW GYROSCOPES

2.1 Gyroscopes Overview

Gyroscopes are simply any devices that measure angular velocity, acceleration, or rotational position. Knowing the acceleration or velocity in the angular axis allows one to calculate the angular orientation by integrating them. In early 1700s gyroscopes were used for sea navigation in foggy conditions and later in 1916, they found their use in aircrafts. Traditional spinning gyroscopes function on the basis that a spinning object that is tilted perpendicularly to the direction of the spin will have a precession. The precession keeps the device oriented in a vertical direction so the angle relative to the reference surface can be measured. Fig. 2.1 shows a spinning gyroscope. Several other kinds of gyroscopes exist - optical gyroscopes, MEMS gyroscopes, etc.

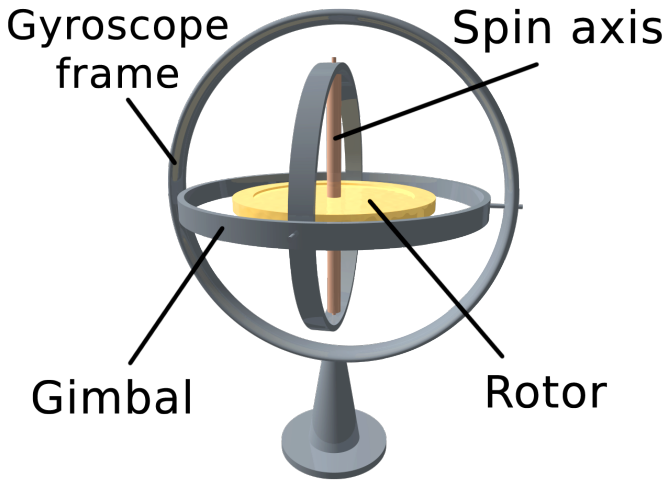

Figure 2.1: 3D illustration of a spinning gyroscope showing the components. Illustration from Wikipedia.

Recently, the move to MEMS gyroscopes has become increasingly common.

MEMS gyroscopes offer the benefits of small size, low power, and low cost which has enabled navigation systems in mobile devices. Even in MEMS gyroscopes there are several kinds - ring laser gyroscopes, tuning fork gyroscopes, etc. However, another class of small, low-power gyroscopes were proposed based on the surface acoustic wave principle by Kurosawa et. al, [12].

SAW gyroscopes are solid state gyroscopes - they have no suspended structures or moving parts. This allows for these gyroscopes to be used in high shock and vibration environments. They are typically made of piezoelectric materials which also have a tolerance for high temperature and other harsh environments. Here, we aim to develop a highly sensitive, high shock tolerant gyroscope which brings us to an obvious solution - SAW gyroscopes.

2.2 Theory of Surface Acoustic Waves

A surface acoustic wave (SAW) is an acoustic wave traveling along the surface of a material that exhibits elasticity. The amplitude of the wave typically decays exponentially into the bulk of the substrate. This phenomenon was first discovered by Lord Rayleigh in 1885 and hence, these waves are also called Rayleigh waves. Fig 2.2 shows a surface acoustic wave. The velocity of these waves varies with materials, and is typically much lower than that of electromagnetic waves. This chapter will explore the analysis of SAW on a piezoelectric substrate and the principle of operation of SAW gyroscopes.

Ever since, SAW phenomenon has been used to design a class of sensors that have been used for sensing various physical phenomenon. A SAW sensor transduces electrical signal into an acoustic signal which is more easily affected

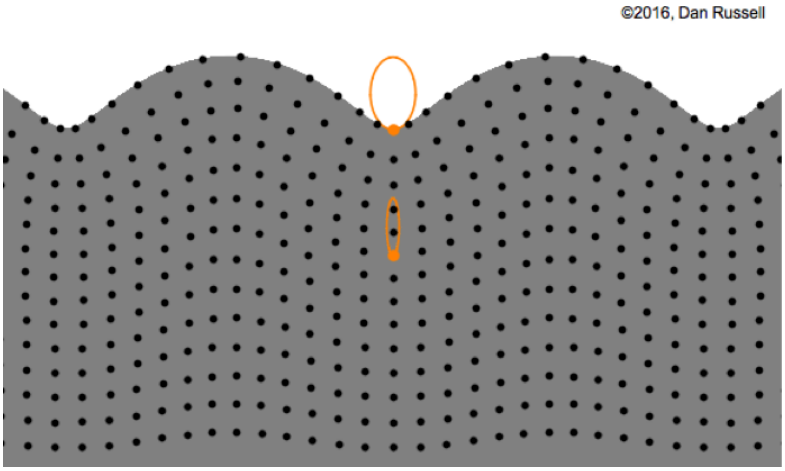

Figure 2.2: A travelling surface acoustic wave

by physical phenomena such as temperature, humidity, pressure, etc and is converted back into an electrical signal. Changes in amplitude, phase, frequency, or time-delay between the input and output electrical signals can be used to measure the presence of the desired phenomenon. Typically, a delay line/resonator structure as shown in Fig. 2.3 is used for a SAW device.

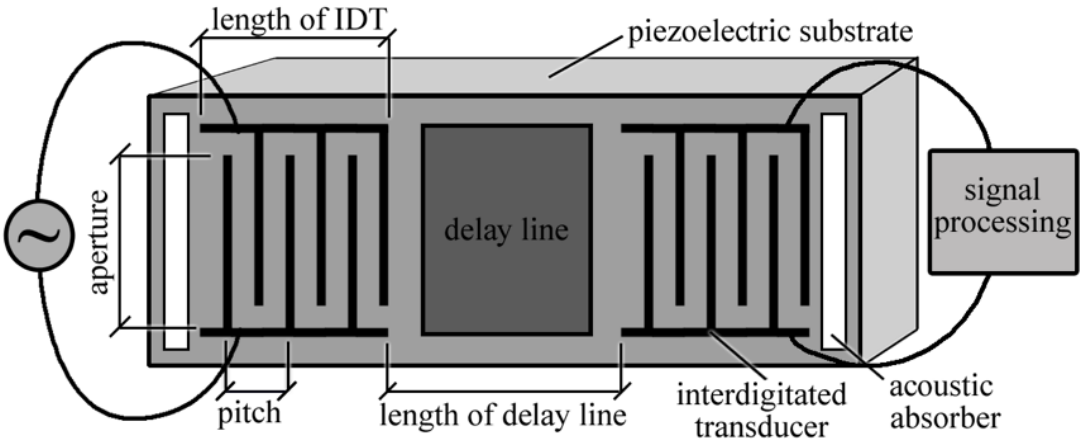

Figure 2.3: A typical SAW delay line

Conventionally, SAW sensors have been used in communications and signal processing as filters for several decades. Recently, due to their low cost, relia-

bility, sensitivity and flexibility, their use in sensing applications has increased greatly. SAW sensors to measure strain, temperature, pressure, mass, acceleration, viscosity have become common. SAW devices are preferred for their high performance, small size and robustness. They are passive devices and can operate in high shock environments, high temperatures and other harsh environments. [13],[14], [15]. Table 2.1 shows some typical sensitivities of various SAW sensors.

Table 2.1: Linear coefficients for physical effects on SAW sensors [16]

Physical Quantity	**Linear Coefficient**
Temperature	up to 100 ppm/K
Pressure, stress	2 ppm/kPa
Mass loading	30 ppm/μg·cm^2
Force	10 ppm/kN
Voltage	1 ppm/V
Electric field	30 ppm/V $\cdot\mu$ m^{-1}

2.3 Analysis of Surface Acoustic Waves - Equations of Motion

When atoms in an elastic medium are subjected to strain, a strong restoring internal force tries to bring the displaced atoms back to their equilibrium positions. This creates a stress causing strain in the medium at a distant point, which in turn creates stress again. This basically results in the propagation of strain in the medium. Surface Acoustic Waves propagate by a similar phenomenon.

Lord Rayleigh proposed a theory for the surface wave, which shows that

it consists of a mixture of shear and longitudinal stress components. Let us first consider a isotropic medium that is in an equilibrium state located at x = x_1, x_2, x_3 which undergoes a displacement by an amount u = u_1, u_2, u_3, where u_1, u_2 and u_3 are functions of x_1, x_2 and x_3. The strain tensor in the medium can now be defined as,

$$S_{ij}(x_1, x_2, x_3) = \frac{1}{2}\left(\frac{\partial u_i}{\partial x_j} + \frac{\partial u_j}{\partial x_i}\right) \qquad i, j = 1,2,3 \tag{2.1}$$

Assuming that the resultant stress, T_{ij} is proportional to the strain given in the previous equation,

$$T_{ij} = \sum_k \sum_l c_{ijkl} S_{kl} \qquad i, j, k, l = 1, 2, 3 \tag{2.2}$$

where c_{ijkl} is the stiffness tensor. In case of piezoelectric materials, there is an asymmetry in the arrangement of the atomic dipoles such that a strain causes polarization charges to appear. Hence, in piezoelectric materials, the strain and electric fields are coupled by a piezoelectric constant, e to give us the constitutive relations:

$$T = cS - e^T E \tag{2.3}$$

$$D = eS + \epsilon E \tag{2.4}$$

Writing equations 2.3 and 2.4 using tensor notations, we get,

$$T_{ij} = \sum_k \sum_l c^E_{ijkl} - \sum_k e_{kij} E_k \qquad i, j, k, l = 1, 2, 3 \tag{2.5}$$

$$D_i = \sum_j \sum_k e_{ijk} S_{jk} + \sum_j \epsilon^S_{ij} E_j \qquad i, j, k, l = 1, 2, 3 \tag{2.6}$$

where $\epsilon^S_{ij}E_j$ is the permittivity tensor at constant strain and e_{ijk} is the piezoelectric constant tensor.

In an isotropic medium, consider an elementary cube of length δ at x = (x_1, x_2, x_3) under a stress S_{ij}, then, the resultant force acting on the cube along the x_1 direction would be

$$F_1 = \delta^2(T_{i1}(x_1 + \delta/2, x_2, x_3) - T_{i1}(x_1 - \delta/2, x_2, x_3)) \tag{2.7}$$

Similarly, we can write forces in x_2 and x_3 directions and combined to write the total force as,

$$F_i = \delta^3\left(\sum_j \frac{\partial T_{ij}}{\partial x_{ij}}\right) \qquad i, j = 1, 2, 3 \tag{2.8}$$

For a material of density ρ, Newton's law of motion given us,

$$\rho\frac{\partial^2 u_i}{\partial t^2} = \sum_j \frac{\partial T_{ij}}{\partial x_{ij}} \qquad i, j = 1, 2, 3 \tag{2.9}$$

In surface waves, the motion is restricted to just one plane, which is usually called the sagittal plane. Fig. 2.4 shows a schematic of the chosen axis and the sagittal plane. The wave is propogating in the x_1 direction. The sagittal plane can now be defined the plane made by the x_1 and x_3 vectors. In an infinite medium, we can define a plane wave to be of the form,

$$u = u_0 exp(j(\omega t - k.x)) \tag{2.10}$$

$$\phi = \phi_0 exp(j(\omega t - k.x)) \tag{2.11}$$

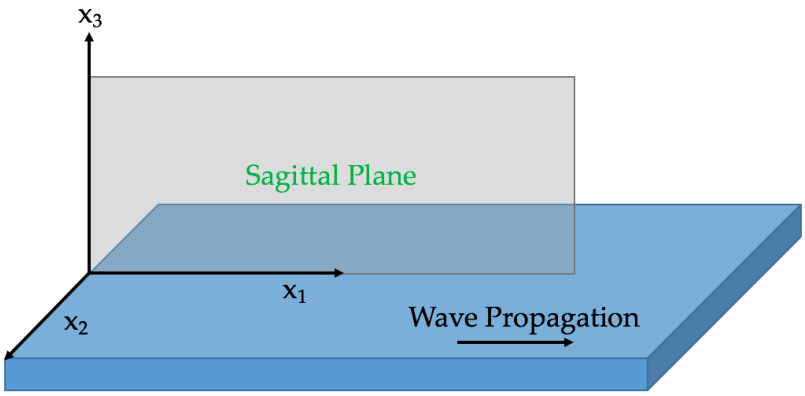

Figure 2.4: Schematic showing the sagittal plane and direction of wave propagation

where u_0 and ϕ_0 are some constants, ω is the wave frequency and k is the wave vector that defines the direction of wave propagation.

Equations 2.10 and are simply solutions of equation 2.9, and we can obtain the solutions by applying appropriate boundary conditions. For our case of a piezoelectric surface, let us consider the medium above the surface to be vacuum. The first boundary condition that follows is that the net force acting on the surface must be equal to zero, i.e,

$$T_{13} = T_{23} = T_{33} = 0 \qquad \text{at } x_3 = 0 \tag{2.12}$$

The second boundary condition is that D_3 should be continuous at the interface of the surface and the vacuum. This gives us,

$$D_3 = \epsilon|\beta|\phi \qquad \text{at } x_3 = 0 \tag{2.13}$$

where ϵ_0 is the permittivity of free space, β is the wave number and ϕ is the potential in vacuum. We can write this potential as,

$$\phi = f(x_3)exp(j(\omega t - \beta x_1)) \tag{2.14}$$

This equation should satisfy Laplace's equation, i.e $\nabla^2\phi = 0$, and it should vanish at $x_3 = \infty$. With these conditions, we can write the potential ϕ in the following form:

$$\phi = \phi_0 exp(-|\beta|x_3)exp(j(\omega t - \beta x_1) \tag{2.15}$$

Now, substituting $E_i = -\partial\phi/\partial x_i$, where ϕ is the electric potential into equation 2.3, reduces the equation of motion in equation 2.9 to

$$\rho\frac{\partial^2 u_i}{\partial t^2} = \sum_j \sum_k \left(\sum_l c^E_{ijkl}\frac{\partial^2 u_k}{\partial x_j \partial x_l} + e_{kij}\frac{\partial^2 \phi}{\partial x_j \partial x_k} \right) \tag{2.16}$$

Since the material we have considered here is a piezoelectric material which is an insulator, the principle of conservation of charge reduces equation 2.4 to

$$\sum_i \sum_j \left(\varepsilon^S_{ij}\frac{\partial^2 \phi}{\partial x_i \partial x_j} + \sum_k e_{kij}\frac{\partial^2 u_j}{\partial x_i \partial x_k} \right) \tag{2.17}$$

To find the solution for surface waves, we have to consider the waves that satisfy the equation of motion for an infinite material given by equations 2.16 and 2.17. We can write the equations for these waves as

$$u' = u'_0 exp(j\gamma x_3)exp(j(\omega t - \beta x_1)) \tag{2.18}$$

$$\phi' = \phi'_0 exp(j\gamma x_3)exp(j(\omega t - \beta x_1)) \tag{2.19}$$

where β is assumed to be real, and γ is a function of v_R/v_T (v_R and v_T being the velocities of Rayleigh and transverse waves respectively.)

The final solution of the equation of motion can be written as a linear combination of partial waves given by

$$u = \sum_{m=1}^{4} A_m u'_m \tag{2.20}$$

$$\phi = \sum_{m=1}^{4} A_m \phi'_m \tag{2.21}$$

where the coefficients A_m satisfy the boundary conditions mentioned in equations 2.12 and 2.13

2.4 SAW Gyroscopes

Based on the principle of surface acoustic wave, Kurosawa, et. al, [12] proposed the first SAW gyroscope. Using a two dimensional construction like SAW filters on a piezoelectric substrate, a novel gyro was proposed. The principle of a SAW gyro is as follows.

A standing wave is generated on an elastic material surface when two propogating SAW are combined. When the substrate is roated, a Coriolis force acts on the particles. The particle vibration velocity is proportional to the primary SAW. A secondary SAW is generated in a direction orthogonal to the primary SAW. Provided the particle velocity is constant, the amplitude of this secondary wave is proportional to the angular velocity. By detecting the strength of the secondary SAW, the magnitude of the corilois force can be measured. From this, the angular rate can be obtained.

However, these coriolis forces cancel each other because of the distribution.

If the cancellation can be avoided and only in-phase secondary waves can be generated, the angular velocity can be obtained. To achieve this, coriolis masses can be placed on the substrate surface at specific locations. These locations are essentially the anti-nodes of the primary standing wave. The forces acting at these points is now stronger than the forces acting on the locations without the masses, and a strong, in-phase secondary wave is generated. Fig. 2.5 depicts the principle of SAW gyroscopes.

Subsequently, several other efforts were made to develop SAW gyroscopes. Table 2.2 compares some existing gyroscopes. Traditionally, SAW gyroscopes detect a change in SAW velocity as a function of the angular rate applied on the device. However, in the proposed work, we detect change in amplitude of the SAW as a function of the angular rate.

Table 2.2: Comparison of previous SAW gyroscopes [17]

Author	**Size(Substrate)**	**Frequency(MHz)**	**(Sensitivity)**
Kurosawa et al.	- ($128^{\circ}LiNbO_3$)	15	-
Varadan et al.	1×1 mm^2 ($128^{\circ}LiNbO_3$)	74.2	705 $\mu V/deg/s$
Wang et al.	1.2×0.75 mm^2 ($128^{\circ}LiNbO_3$)	80	119 $Hz/deg/s$
Oh et al.	1.2×0.8 mm^2 ($128^{\circ}LiNbO_3$)	80	1.23 $deg/deg/s$
Lee et al.	($128^{\circ}LiNbO_3$)	80/160	27.5 $\mu V/deg/s$

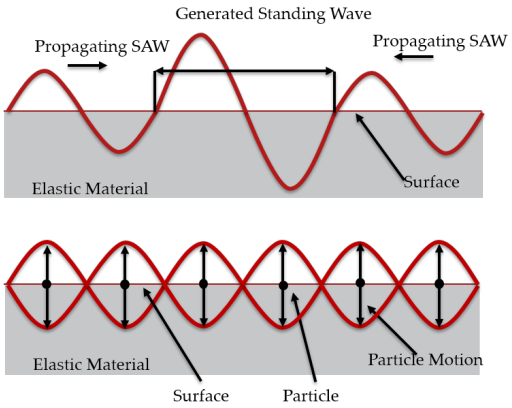

(a) Standing Wave generation on an elastic material

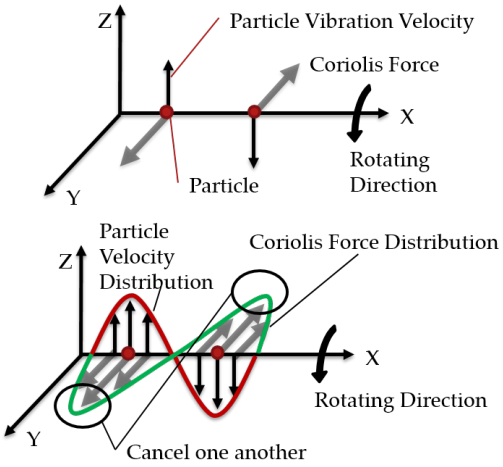

(b) Secondary SAW generation due to Coriolis forces

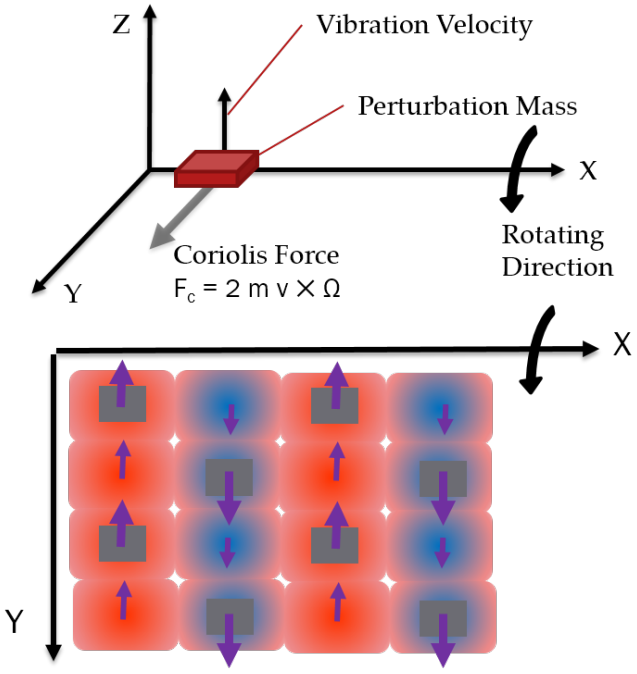

(c) Addition of coriolis masses at anti-nodes of primary standing wave

Figure 2.5: Principle of SAW gyroscopes

CHAPTER 3

DESIGN AND EXPERIMENTAL SETUP

3.1 Device Design

Typically, SAW gyroscopes have a two resonator structures with a cavity consisting of a metallic pillar arrangement. The resonator structures can be either one port or two port, depending on the configuration. We chose the two port configuration because it allows for closed loop feedback SAW oscillator. Fig. 3.1 shows an illustration of the gyro in this work. The gyro design can broadly be divided into the following sub-components

- Piezoelectric Substrate Selection
- SAW Resonator Design
- Metallic Pillar Array Design

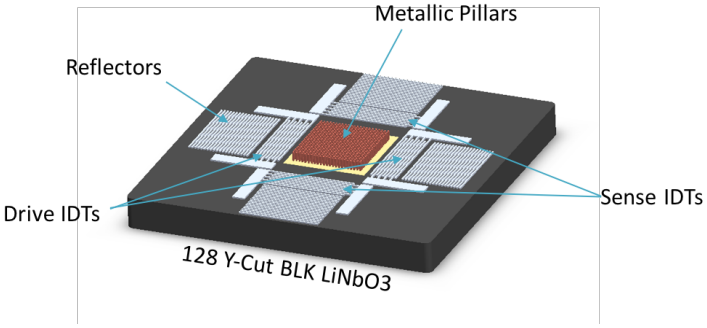

Figure 3.1: Illustration of the SAW gyroscope proposed in this work

3.1.1 Piezoelectric Substrate Selection

The selection of a suitable piezoelectric substrate is important for a SAW device because its behaviour is strongly dependent on the properties of the material. Typical piezoelectric materials used in SAW devices include Quartz, Lithium Niobate, Aluminum Nitride and PZT (Lead Zirconium Titrate).

In this work, we chose 128 °Y cut Lithium Niobate ($LiNbo_3$) because of it's high electromechanical coupling coefficient (K^2 = 5.3%) In order to reduce fabrication complexities, black Lithium Niobate wafers with reduced pyroelectric coefficient were used.

3.1.2 SAW Resonator Design

A two port SAW resonator design has two sets of identical IDTs and reflectors. Each set of IDTs are placed at the opposite ends of a resonance cavity between several reflectors. The reflectors help setup a standing wave by reflecting maximum amount of the energy back into the cavity. The choice of the optimal spacing between the IDTs to the reflecting fingers (L_{rt}) will result in the maximum coupling to the cavity. [18] Table 3.1 shows the design parameters of the resonator structures.

3.1.3 Metallic Pillar Array

The cavity design and pillar alignment involves the design of cavity spacing, alignment of the pillars/Coriolis masses in the cavity to ensure the generation

Table 3.1: SAW Gyroscope Resonator Design Parameters

	Drive Axis (x)	Sense Axis (y)
IDT Finger pairs	5	5
Reflectors	300	300
Wavelength	19.17	17.91
Cavity Length	$90\lambda_x$	$90\lambda_y$
L_{rt}	$\lambda_x/2$	$\lambda_y/2$

of a secondary SAW for measuring the angular rate. The length of the acoustic cavity is chosen to accommodate the acoustic aperture of sense resonator and the Coriolis masses. The Coriolis masses are placed in the acoustic cavity between two IDTs. For symmetric mode cavity, the length of acoustic cavity needs to be $l_c = (2n)\lambda$. The symmetric mode (positive antinode at the center of cavity) is selected over antisymmetric (node at the center of cavity) mode to assist in the distribution of the Coriolis masses in both the directions. Fig. 3.2 shows the alignment of the pillars.

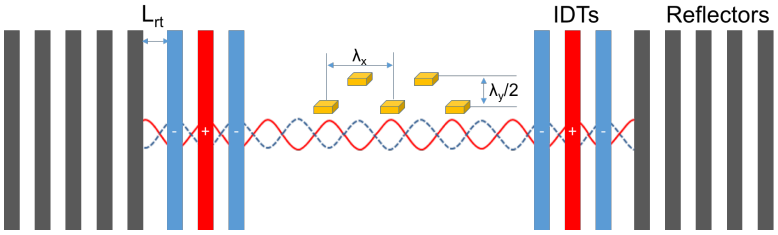

Figure 3.2: Coriolis Masses placed at positive antinode of the standing wave in a symmetric SAW resonator cavity.

The reflector array and Coriolis masses in the cavity will cause a decay of phase velocity due to the mass loading. The optimal alignment of metallic pillars to the positive antinodes of velocity in drive axis (x-direction) requires compensation for change in phase velocity. Three cycles of iterative design-of-experiment (DOE) (Fig. 3.3) steps were used for compensation. In each step the

measured correction factor was used for updating the next step. Similar consideration applies for placement of dots in sense axis with an exception of $\lambda/2$ pitch in y-direction.

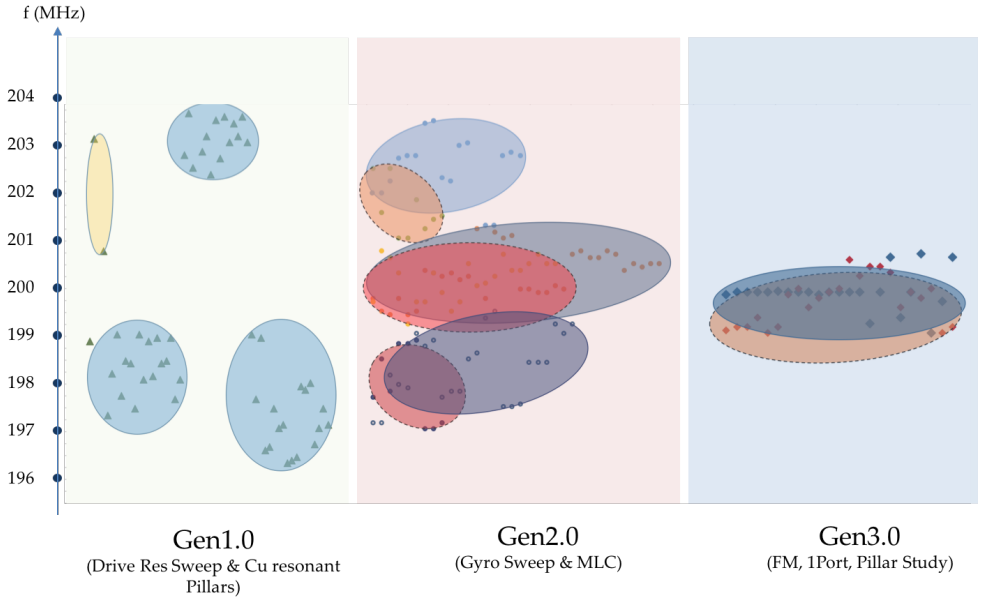

Figure 3.3: Summary of the Design of Experiment process to achieve frequency matching

3.2 Graphene Devices

3.2.1 Test Devices

Several device designs were tested to understand graphene response. The layout of two such devices are shown in Fig. 3.4 and Fig. 3.5.

The device shown in Fig. 3.4 was designed to test the response of graphene by varying the length of the graphene resistor across the two gold electrodes. Three configurations were tested: λ, $\lambda/2$ and $\lambda/4$. Device shown in Fig. 3.5

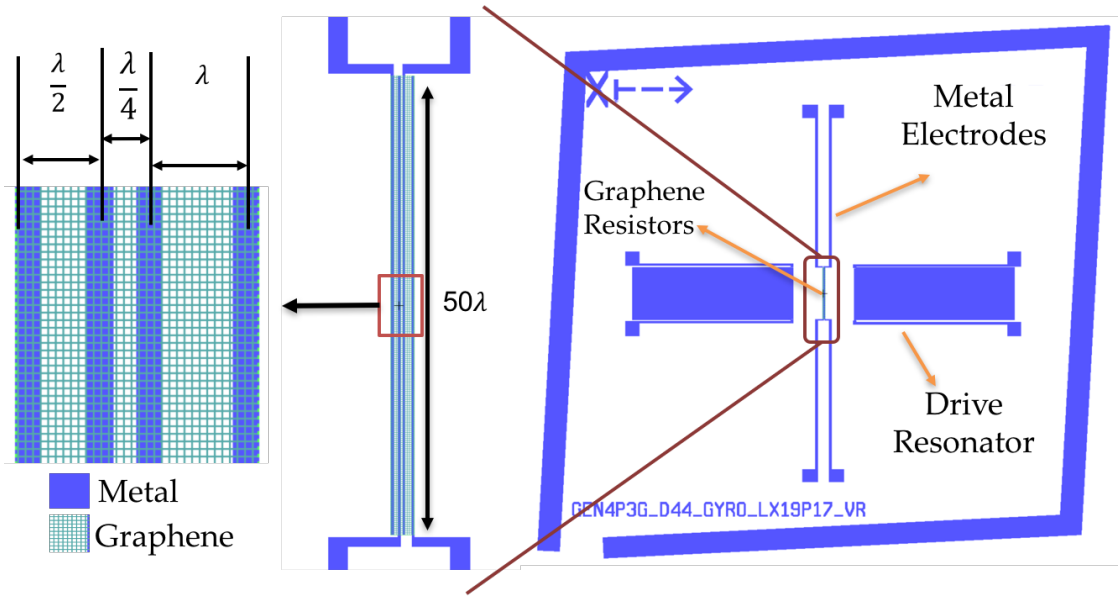

Figure 3.4: Layout of VR - Test device

varied the width of the graphene resistor keeping the length constant. Table 3.2 shows the DC resistances of the devices, measured using Keithley 6430 SMU.

Device	DC Resistance (R_0)
VR - λ	160Ω
VR - $\lambda/2$	196Ω
VR - $\lambda/4$	208Ω
Gyroscope Device	12.08kΩ

Table 3.2: DC Resistances of various Graphene Devices

3.2.2 Gyroscope Device

A SAW gyroscope with graphene pickups was also designed as shown in Fig. 3.6. The DC resistance of the graphene was measured to be 12.08kΩ. The drive port of the device has a resonator structure which has a S_{21} parameter as shown

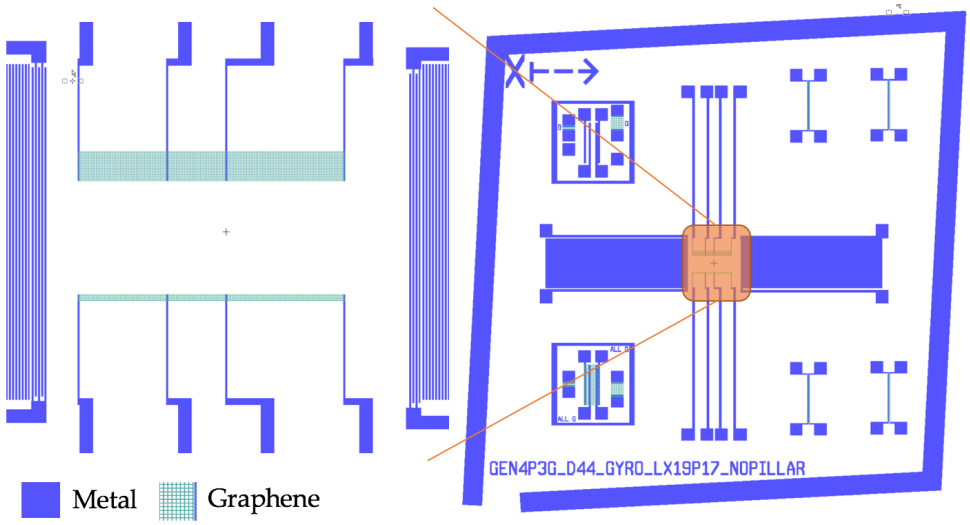

Figure 3.5: Layout of GW - Test device

in Fig. 4.6. The fundamental resonance was found to be at 200.177 MHz which is close to the designed frequency of 200 MHz. Raman spectroscopy was utilized to ensure graphene quality after transferring to and processing on the LiNbO3 substrate.

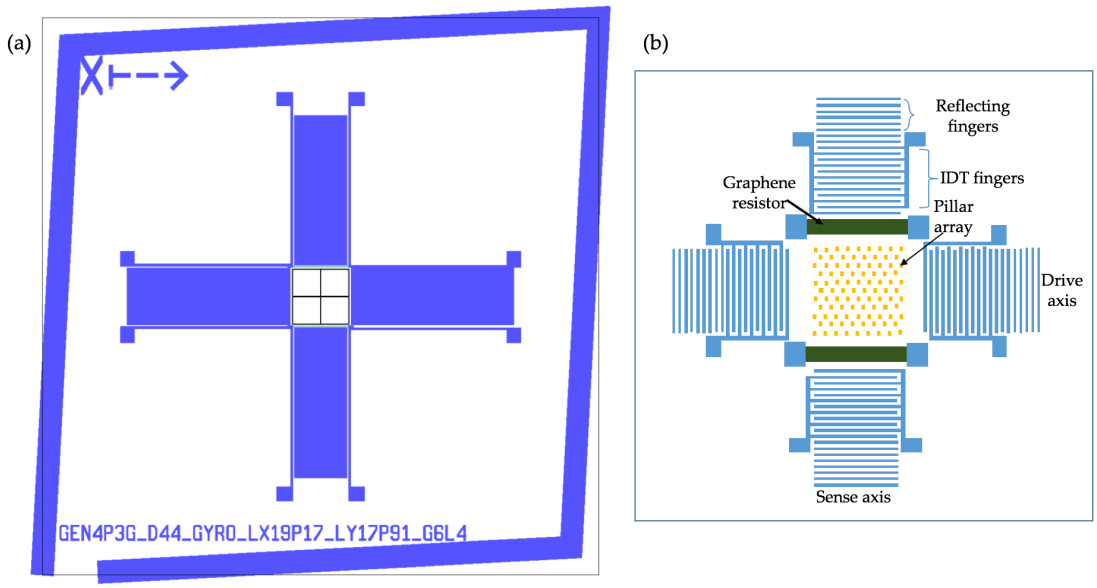

Figure 3.6: (a) Layout and (b) Schematic of SAW Gyroscope with Graphene Transducer

3.3 Experimental Apparatus

The experimental setup for biasing the graphene is shown in Fig. 3.7. A Keithley 6430 sub-femto amp current meter was used to bias and measure the current across graphene. The SAW was excited using a Agilent E8257C RF Signal generator. The entire process was automated using a python script that communicated to both the instrument over GPIB. The Keithley 6430 requires a remote pre-amp to enable sub-nanoamp current measurement. The current was measured with an NPLC (number of power lines per cycle) of 10 to achieve maximum accuracy.

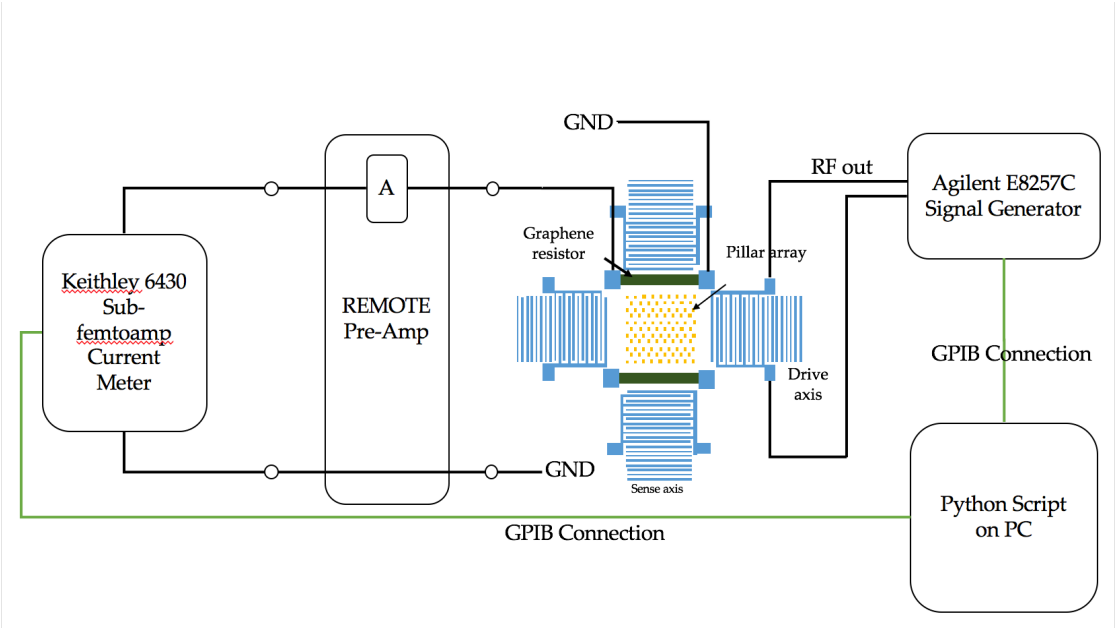

Figure 3.7: Experimental Setup for Graphene Bias and Current measurement

Automation of the process allowed the experiment to be repeated for several range of frequencies, multiple voltage biases for many devices.

CHAPTER 4

RESULTS AND DISCUSSION

4.1 Response of Graphene in test device

The graphene response when various RF drive voltages are applied is shown in Fig. 4.1. We observed the acoustoelectric effect - a DC current as a result of the SAW. At frequencies lesser or greater than the resonance frequencies of the drive resonator, the DC current remains fairly constant at a level = V_{bias}/R_0, where V_{bias} is the bias voltage across the graphene and R_0 is the DC resistance of the piezoresistor. However, the response at the resonance frequencies of the drive is interesting - it either has a local maxima or local minima.

Results were recorded by varying the bias voltage across graphene for the three different configurations of VR device. Three different bias voltages were applied - starting with 0V, and then 100 μV and -100 μV. The insertion loss (S_{21}) of the drive resonator was measured using an Agilent E5061b Vector Network Analyzer and is shown in Fig. 4.2. There are three split-resonance peaks at $\sim$ 199.55 MHz, $\sim$ 200.7 MHz and $\sim$ 201.85 MHz. However, when all of these curves are normalized (divided by the average DC current at a respective bias level) and plotted on the same graph, we get Fig. 4.3. The percentage change in current at our resonant frequency for this device, $\sim$ 200.7 MHz, we can observe that the maximum percentage change in the current at resonance happens in the λ /4 configuration. The change decreases as the width of the graphene decreases, as shown in Fig. 4.4.

In order to obtain maximum $\Delta R/R$, we need to bias the graphene close to

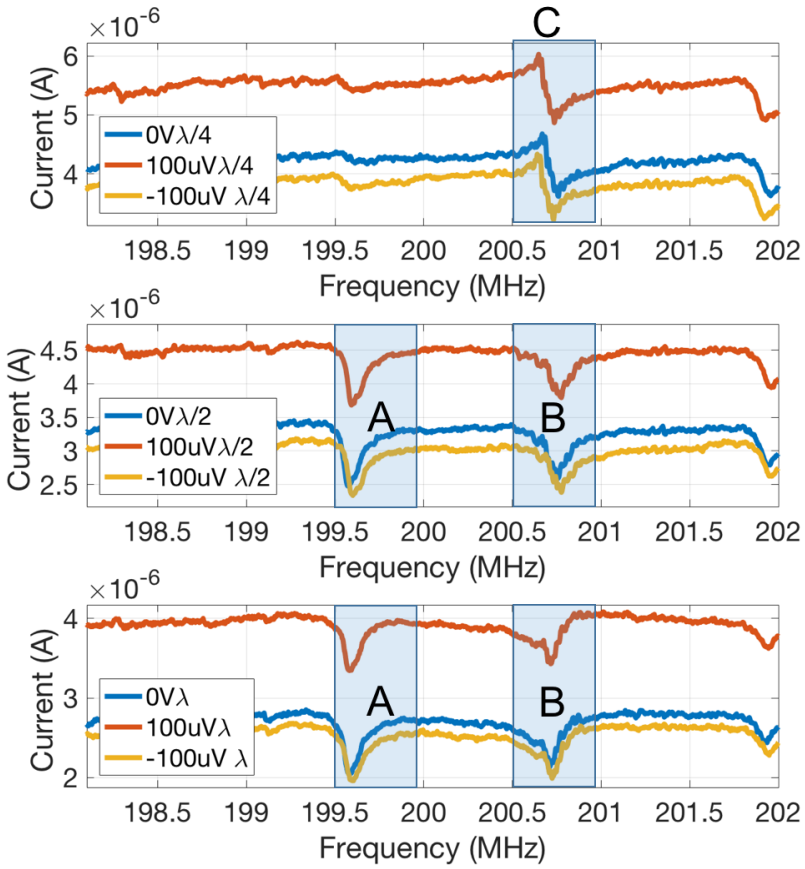

Figure 4.1: RF response of graphene in test device for varying bias voltages, RF power 3V

the zero crossing / zero current point. In the devices of width λ and $\lambda/2$ we observe that there are two regions of interest, indicated by A and B in Fig. 4.1. However, the $\lambda/4$ resistor has only one resonance region indicated by C in Fig. 4.1. This frequency corresponds to the resonance frequency of the drive in this device (Fig. 4.2). Hence, we try to bias the $\lambda/4$ device as shown in Fig. 4.5 to achieve maximum sensitivity.

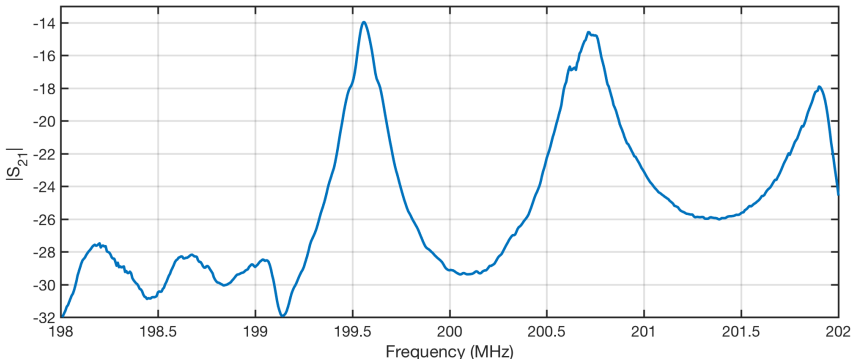

Figure 4.2: S_{21} curve for the drive resonator of VR test device

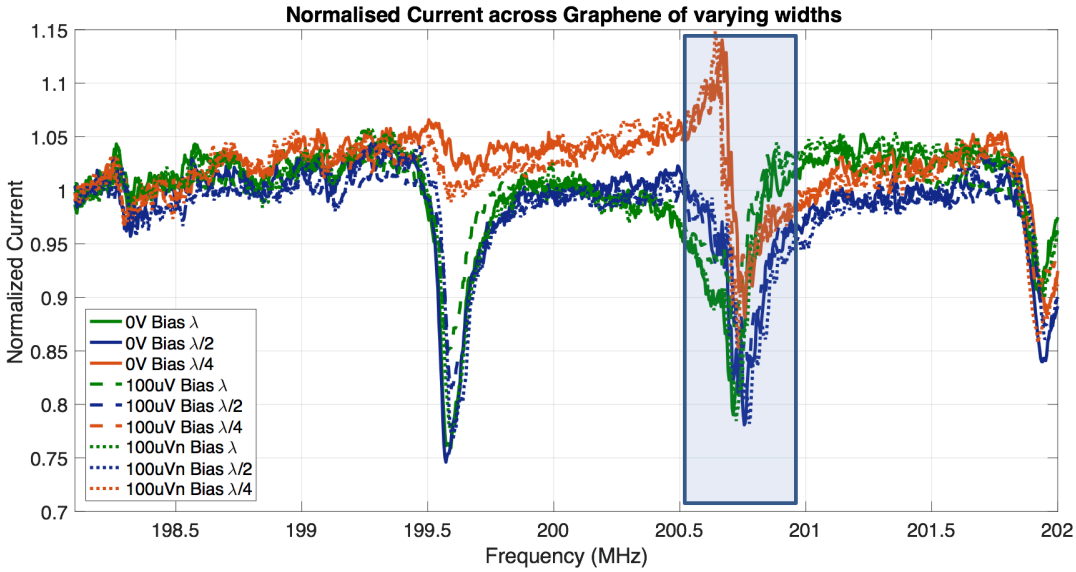

Figure 4.3: Normalised current across graphene in test device for various bias voltages

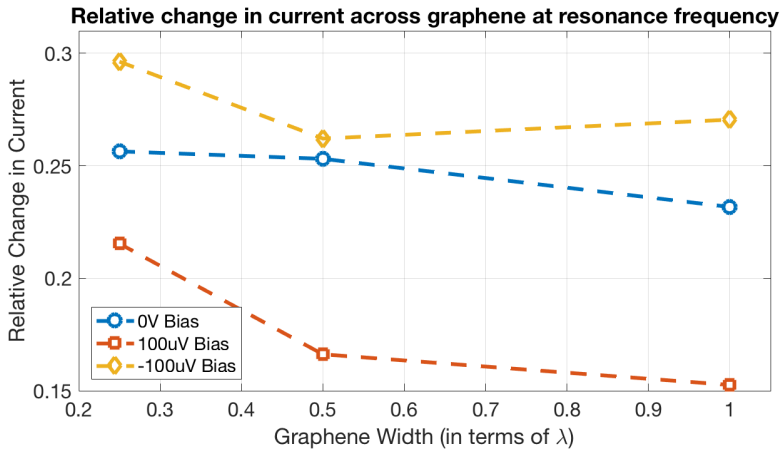

Figure 4.4: Relative change of normalised current across graphene in test device for various bias voltages

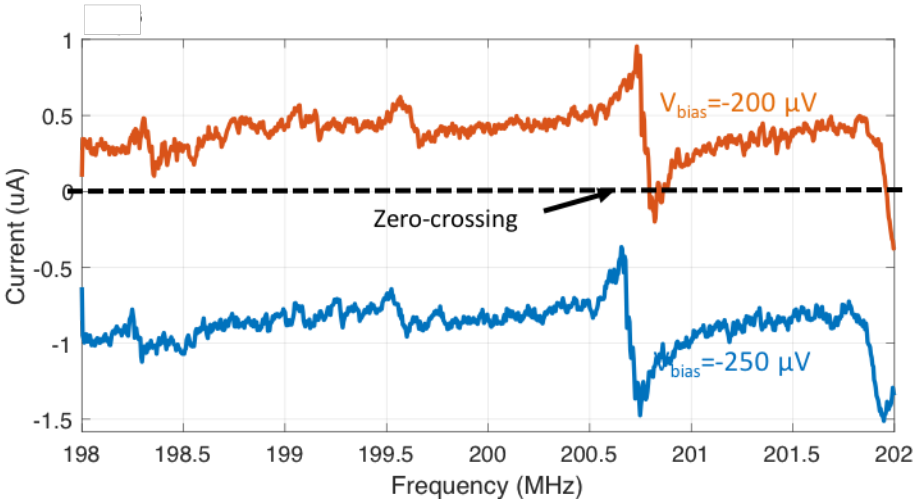

Figure 4.5: Biasing the $\lambda/4$ resistor close to the zero crossing to obtain high $\Delta R/\mathrm{R}$

4.2 Response of graphene transducer in Gyroscope device

A graphene transducer was fabricated outside the cavity to act as a pickup for a SAW gyroscope instead of regular metal IDTs. The insertion loss of the drive resonator for the device is plotted in Fig. 4.6. Similar to VR device, there is a split-resonance peak. The global maxima is close to 200.18 MHz. The DC current across the pickup due to the scattering SAW was measured for three different RF drive voltages. The entire process was repeated for several bias voltages. The results of the experiment are plotted in Fig. 4.7. As expected, all the curves for a particular bias voltage are centered around the same DC value. An increasing RF power in the drive port results in a more stronger response at resonance.

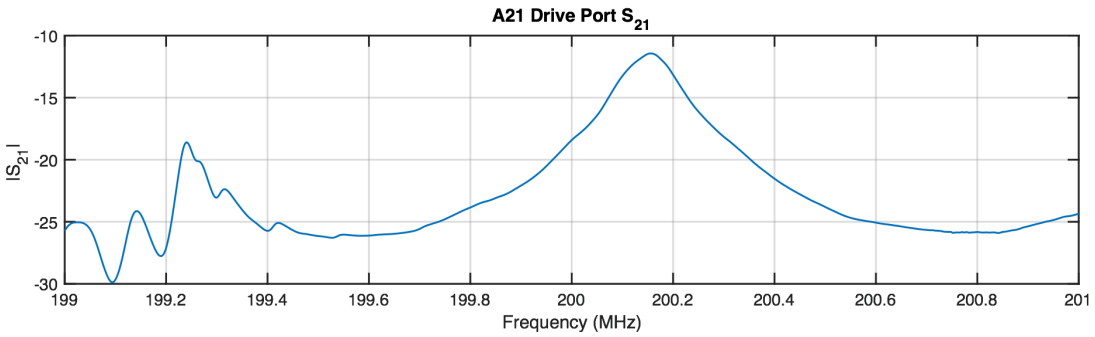

Figure 4.6: S_{21} parameter curve for drive resonator

We can see three regions of interest in the plot in Fig. 4.7. An initial peak, a valley followed by a peak. However, when bias voltages of much larger magnitude were applied, the two peaks disappear as shown in Fig. 4.8. A more prominent aspect is that the valley at resonance inverts and becomes a peak.

The raw data obtained from Fig. 4.8 was processed to obtain figures 4.9 and 4.10. The baseline current was taken as the average of the first 100 data points

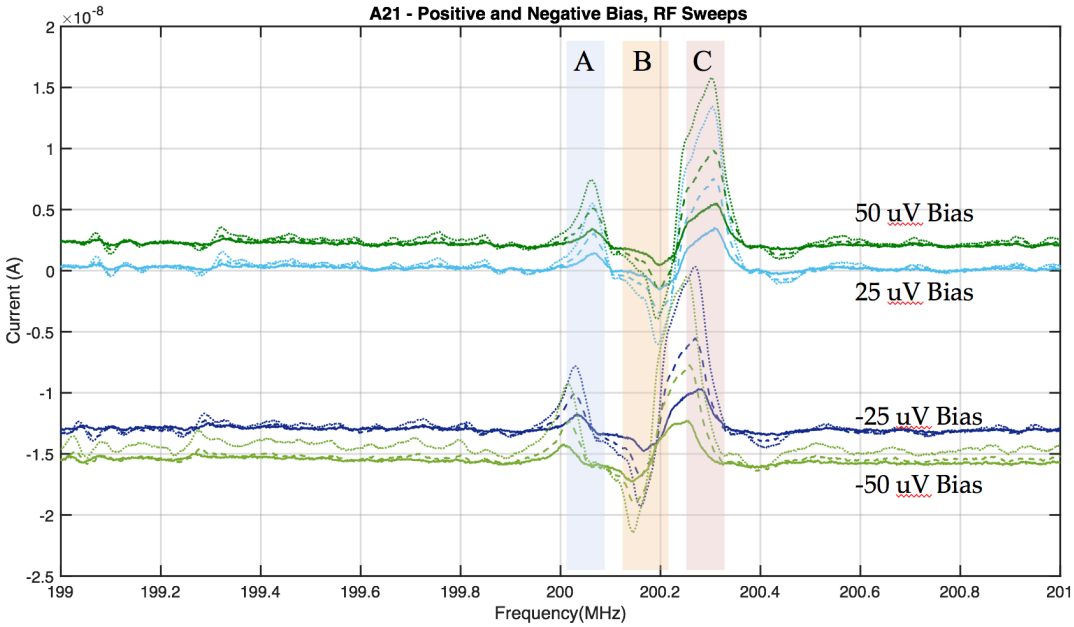

Figure 4.7: DC response of graphene on Gyro device for varying bias voltages for 3 different RF powers

from Fig. 4.8. The resonance current is taken to be the maximum/minimum current at resonance.

4.3 Effective Resistance of Graphene

Instead of using discrete resistors for a piezoresistance measurement, an instantaneous point by point calculation to find a perceived resistance and change in resistance at a given data acquisition is utilized. Doing this allows for very large apparent ΔR values to be obtained despite the physical graphene resistance remaining constant. We can define the instantaneous resistance of the graphene to be,

$$R_G = \frac{V_D}{I_D - I_{SAW} - I_{gyro}} \tag{4.1}$$

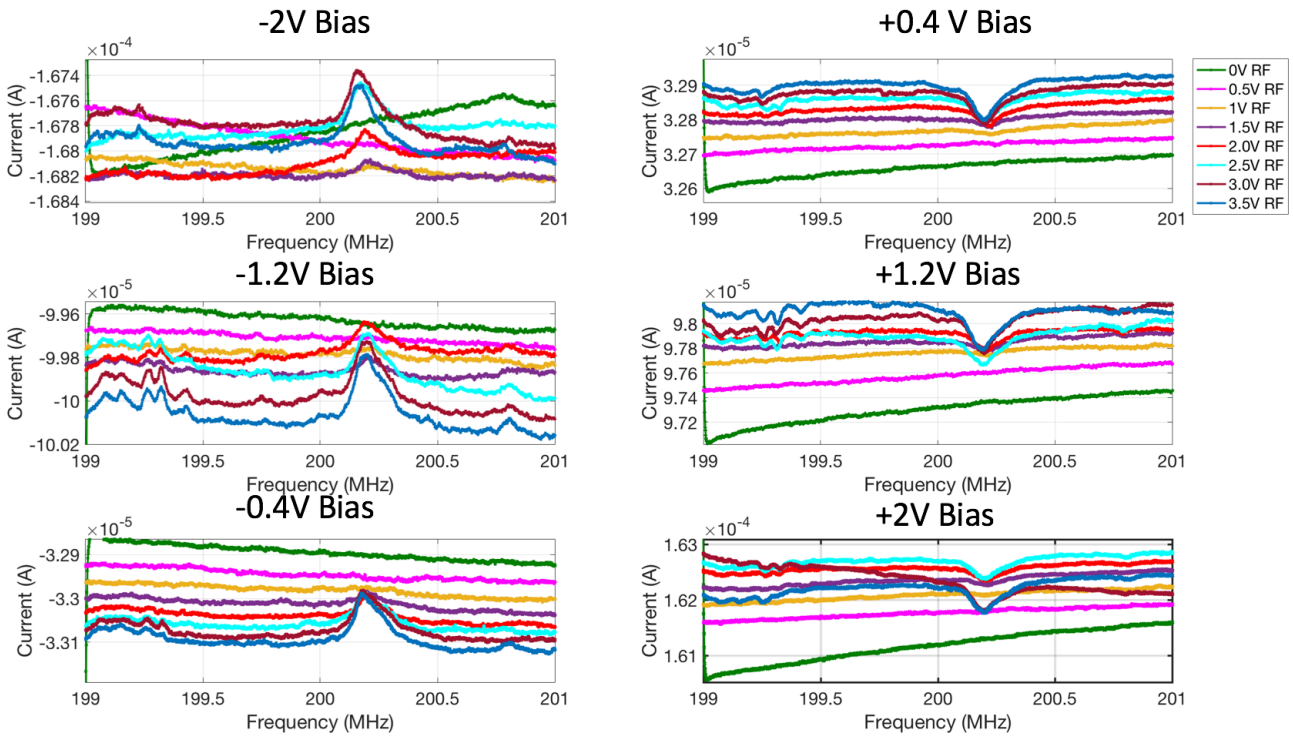

Figure 4.8: Large bias voltage response of graphene

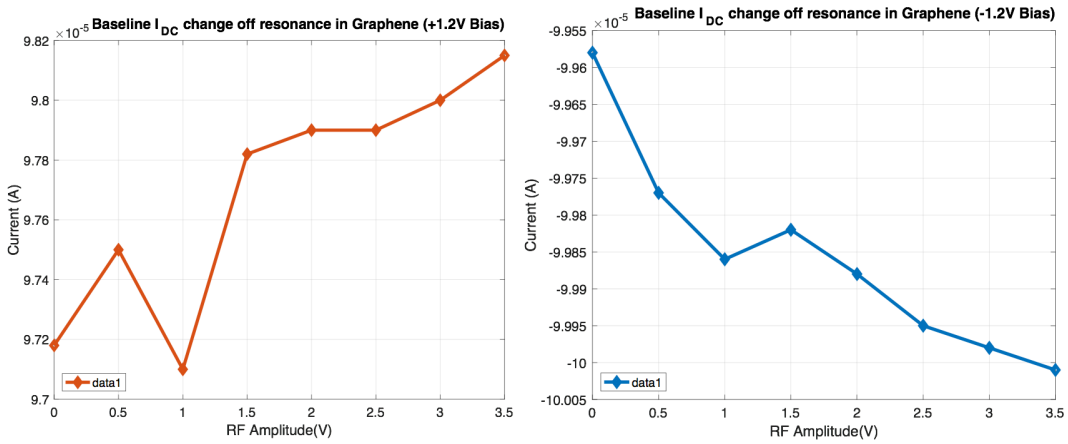

Figure 4.9: Variation in baseline current due to bias voltage

where V_D denotes the DC bias voltage across the graphene, I_D denotes the DC current due to the bias, I_{SAW} denotes the DC current due to the primary SAW scattering and I_{gyro} denotes the DC current due the secondary SAW generated by rotation.

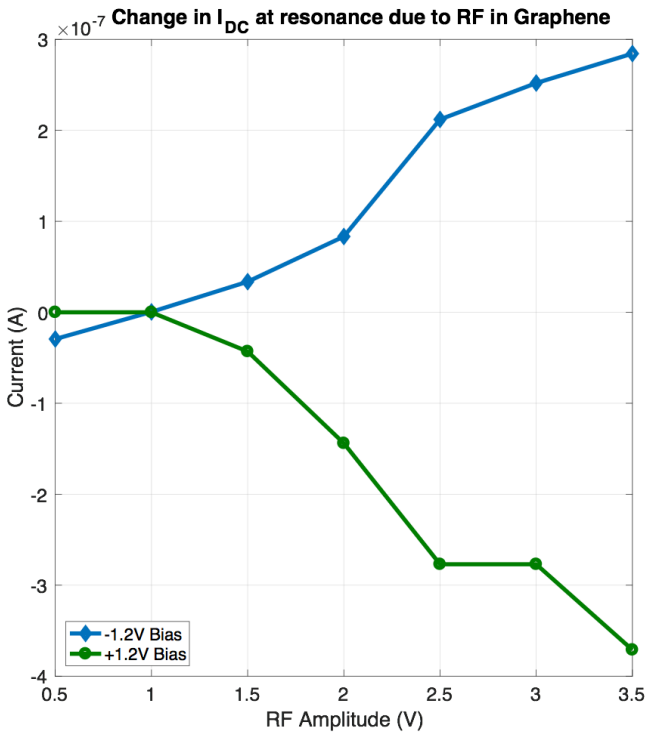

Figure 4.10: Variation in peak current at resonance due to bias voltage

The change in resistance can be written as,

$$\frac{\Delta R}{R} = \frac{R_G - R_0}{R_0} \tag{4.2}$$

From this, instantaneous $\Delta R/R$ using the graphenes intrinsic DC resistance (R_0) can be plotted, as shown in Fig. 4.11a

4.4 High Gauge factor of Graphene

The differential resistance, or the partial change in resistance with respect to I_{gyro} can be written as,

$$\Delta R = \frac{\partial R}{\partial I_{gyro}} = \frac{V_D}{(I_D - I_{SAW} - I_{gyro})^2} \tag{4.3}$$

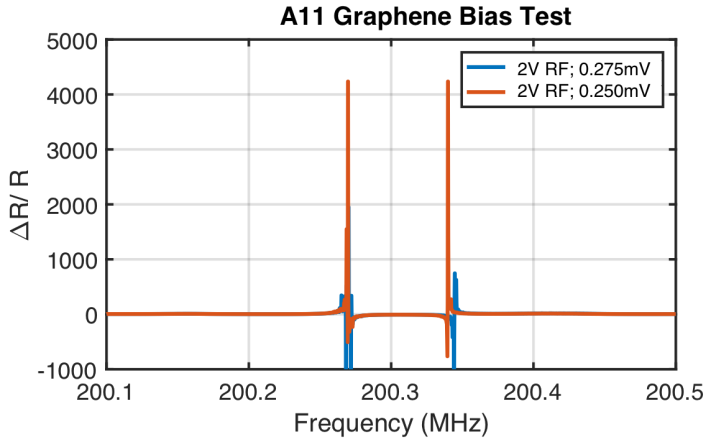

(a) A plot showing $\Delta R/R$ across a range of frequencies for gyro device. Drive RF = 2V and bias voltages were 250µV and 275µV

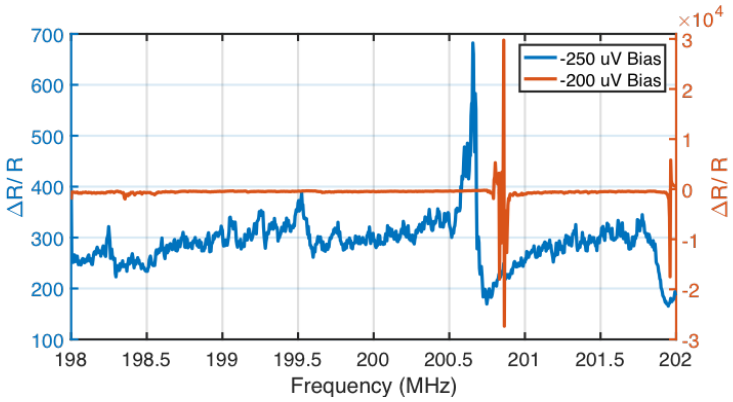

(b) A plot showing $\Delta R/R$ across a range of frequencies for test device. Drive RF = 3V and bias voltages were -250µV and -200µV

Figure 4.11: Tuning bias voltages to achieve high $\Delta R/R$

Let I_S be the DC current due to primary and secondary SAWs,

$$I_S = I_{SAW} + I_{gyro} \tag{4.4}$$

Now, if we tune the bias voltage to keep the DC current due to the bias equal to I_S, we get,

$$\lim_{I_D \to I_S} \frac{\Delta R}{R} = \infty \tag{4.5}$$

which allows us to write the gauge factor of graphene,

$$GF = \frac{\Delta R/R}{\varepsilon} \tag{4.6}$$

$$\frac{\Delta R}{R} \to \infty, GF \to \infty \tag{4.7}$$

A laser Doppler microscope (LDV, Polytec-UHF) was used to measure the SAW displacement over the graphene resistor at the fundamental frequency for various input powers. Fig. 4.12 shows a spatial map of the displacement for an RF drive power of 5V.

Under the assumption of strain continuity across the lithium niobate substrate and graphene resistor, the in-plane nominal strain on the graphene resistor can be written as,

$$\varepsilon_Z = \mathrm{k}|U_{\max}| \tag{4.8}$$

$$= \frac{2\pi}{\lambda} U_{\max} \tag{4.9}$$

$$= \frac{2\pi}{\lambda} \mathrm{A_N} \tag{4.10}$$

where $\mathrm{A_N}$ is the SAW amplitude and λ is the wavelength.

The gauge factor can now be expressed as,

$$GF = \frac{\left(\frac{\Delta R}{R}\right)}{\varepsilon_Z} \tag{4.11}$$

$$= \frac{\left(\frac{\Delta R}{R}\right)}{\left(\frac{2\pi}{\lambda} A_N\right)} \tag{4.12}$$

$$\tag{4.13}$$

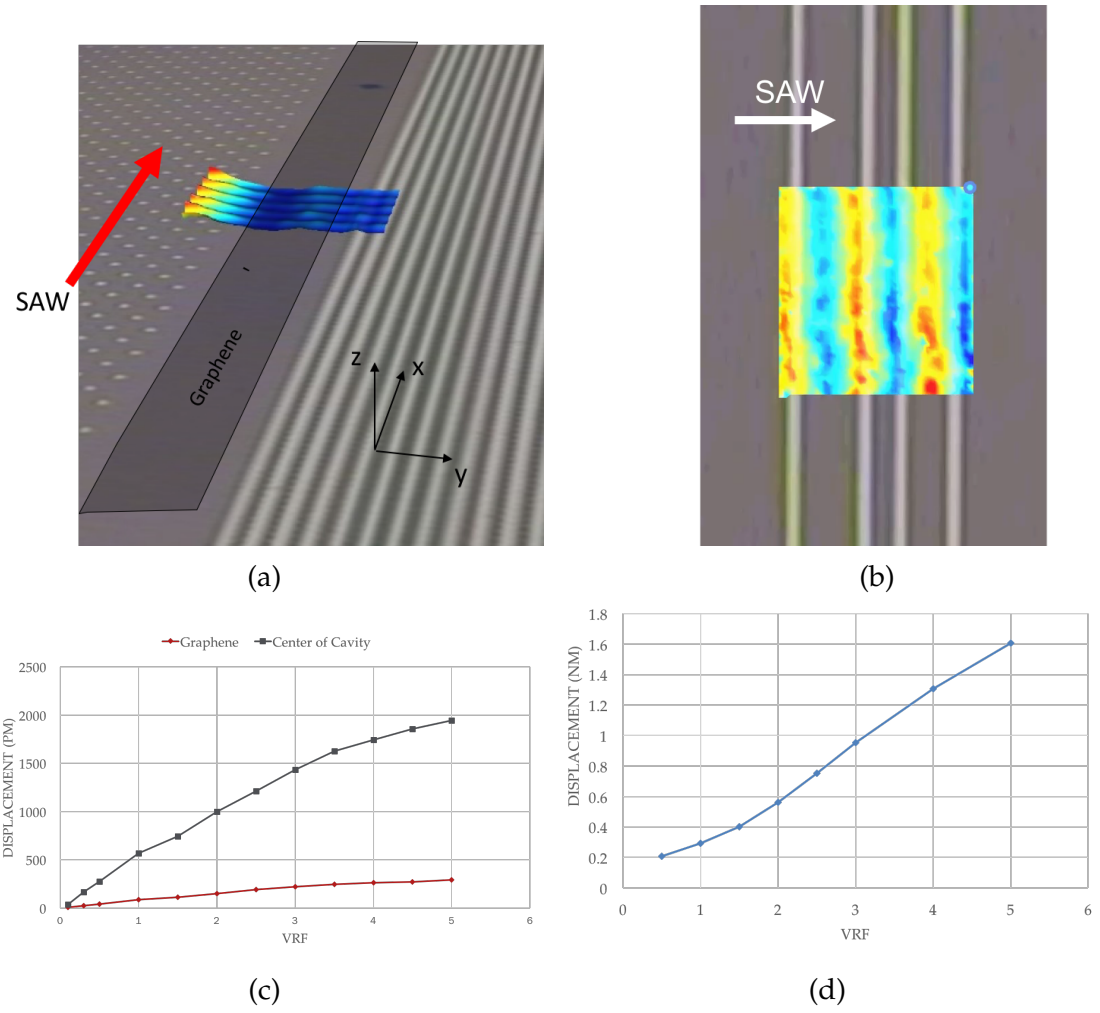

Figure 4.12: Laser Doppler Vibrometer measurement of strain across Graphene test device. (a) and (c) show data for gyroscope device, (b) and (d) show data for the test device.

Plugging in the values for $\Delta R/R$ obtained from Fig. 4.11a, wavelength, λ = 20 µm and the maximum displacement due to the primary SAW, we obtain gauge factor of graphene to be

$$GF = \frac{4000}{\frac{2\pi}{20\mu m}300pm} \tag{4.14}$$

$$GF \approx 4.2 \times 10^6 \tag{4.15}$$

Similar experiments on the test device also resulted in a $\Delta R/R$ of nearly 30,000 as shown in Fig. 4.11b. Plugging in the values of displacement from Fig. 4.12 for the test device, we get,

$$GF = \frac{30000}{\frac{2\pi}{20\mu m}954pm} \tag{4.16}$$

$$GF \approx 1 \times 10^8 \tag{4.17}$$

This high gauge factor is a result of specific biasing of the piezoresistor. In practice, the biasing of the resistor at a given SAW RF power will need to be adjusted in the analog or digital domain, followed by a small signal monitoring of the resistance change. The system can be made highly sensitive by designing a system that can closely mirror the behaviour of I_S.

CHAPTER 5

CONCLUSION AND FUTURE WORK

Measuring SAW amplitudes using traditional IDTs requires RF electronics which is often complex and consumes a large amount of power. Metal IDTs result in mass-loading which can reduce the Q of the resonant cavity. In this work, we fabricated for the first time a transverse acoustoelectric graphene device that produces measurable AE current while leaving the acoustic cavity free of any mass loading structures. We successfully demonstrated that graphene can be used as a SAW transducer. We explored the use of the acoustoelectric effect in graphene to pick up changes in the electrical inputs to the system by utilizing a numerical method for resistance to achieve very high sensitivity. We showed that, a 954 pm displacement at 200.6 MHz at 3V, can lead to a numerical $\Delta R/R$ of at least 30000 and gauge factor of 1×10^8. We characterized the behaviour of graphene in a SAW gyroscope device. With the results of our work, we conclude that graphene resistors show great potential as transducers for SAW sensors. As shown in the last chapter, the graphene electrodes can be chosen to have an output impedance of 50Ω, leading to distinct advantages for both AC and DC coupling the output of the device.

The SAW transducer we have include high sensitivity magnetic sensors, gas sensors, etc. In terms of gyroscope instrumentation, further work is necessary to realize the high sensitivity for measuring the angular rate.

APPENDIX A

CHAPTER 1 OF APPENDIX

The design and fabrication process of all the devices in this work were entirely done by Benyamin Davaji, Post-doctoral associate of SonicMEMS.

The devices were fabricated on 128 °Y-cut black lithium niobate wafers, because of its high electromechanical coupling coefficient. The fabrication process has several steps. The wafers are first cleaned using piranha solution and are dried overnight in an N_2 environment. After cleaning, the patterns are transferred to the substrate by lithography followed by plasma descum process. After the descum process, 200 nm of Au is deposited on the substrate, with 10 nm of Ti used as a bonding layer. This is followed by a liftoff process to get complete the SAW device fabrication process.

The patterns are transferred to the substrate using a lift-off process as shown in Fig. A.1.

After the device had been fabricated, commercially available graphene was transferred to the device followed by lithography. An O_2 plasma was used to etch away the graphene in the unnecessary regions. The final step was to strip the photoresist and the PMMA to retain only graphene. Fig.A.2 shows the graphene transfer process.

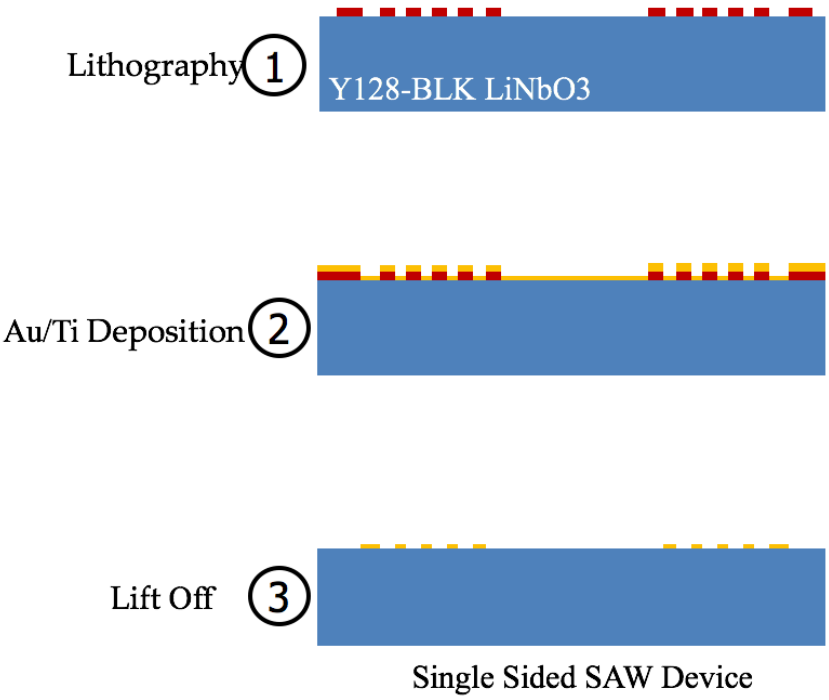

Figure A.1: Fabrication Process: Metal Deposition and Liftoff

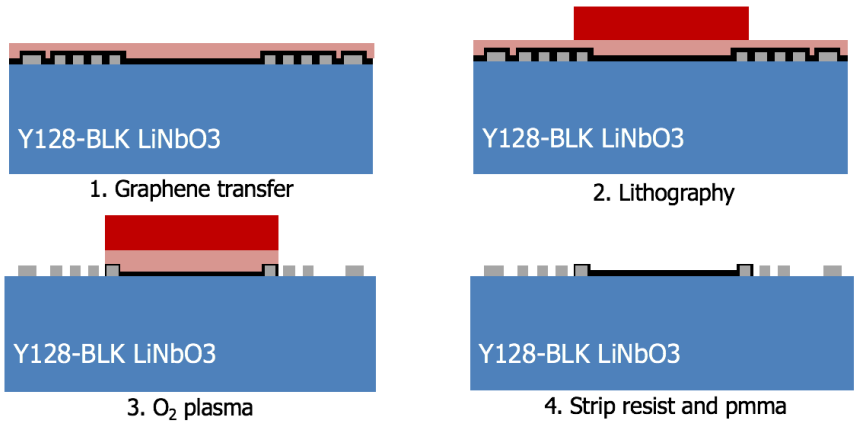

Figure A.2: Fabrication Process: Graphene Transfer

REFERENCES

[1] A. K. Geim and K. S. Novoselov, "The rise of graphene," *Nature Materials*, vol. 6, no. 3, pp. 183–191, 2007.

[2] K. S. Novoselov, A. K. Geim, S. V. Morozov, D. Jiang, Y. Zhang, S. V. Dubonos, I. V. Grigorieva, and A. A. Firsov, "Electric field effect in atomically thin carbon films." *Science (New York, N.Y.)*, vol. 306, no. 5696, pp. 666–9, 2004. [Online]. Available: http://www.ncbi.nlm.nih.gov/pubmed/15499015

[3] D. Čiplys, R. Rimeika, V. Chivukula, M. S. Shur, J. H. Kim, and J. M. Xu, "Surface acoustic waves in graphene structures: Response to ambient humidity," in *Proceedings of IEEE Sensors*, 2010, pp. 785–788.

[4] A. Leong, V. Swamy, and N. Ramakrishnan, "Multilayer graphene electrodes for one-port surface acoustic wave resonator mass sensor," *Japanese Journal of Applied Physics*, vol. 56, no. 2, p. 024301, 2017. [Online]. Available: http://stacks.iop.org/1347-4065/56/i=2/a=024301

[5] V. S. Chivukula, D. Ciplys, Jin Ho Kim, R. Rimeika, J. M. Xu, and M. S. Shur, "Surface acoustic wave response to optical absorption by graphene composite film," *IEEE Transactions on Ultrasonics, Ferroelectrics, and Frequency Control*, vol. 59, no. 2, pp. 265–270, 2012. [Online]. Available: http://ieeexplore.ieee.org/document/6156828/

[6] V. Miseikis, J. E. Cunningham, K. Saeed, R. O'Rorke, and A. G. Davies, "Acoustically induced current flow in graphene," *Applied Physics Letters*, vol. 100, no. 13, 2012.

[7] E. Emelin, Z. Insepov, O. Kononenko, D. Roshchupkin, and K. Tynyshtykbayev, "Amplification of surface acoustic waves in graphene film under DC-voltage," in *Technical Proceedings of the 2014 NSTI Nanotechnology Conference and Expo, NSTI-Nanotech 2014*, vol. 1, 2014.

[8] Z. Qian, F. Liu, Y. Hui, S. Kar, and M. Rinaldi, "Graphene as a Massless Electrode for Ultrahigh-Frequency Piezoelectric Nanoelectromechanical Systems," *Nano Letters*, vol. 15, no. 7, pp. 4599–4604, 2015.

[9] M. M. De Lima, W. Seidel, H. Kostial, and P. V. Santos, "Embedded Interdigital transducers for high-frequency surface acoustic waves on GaAs," *Journal of Applied Physics*, vol. 96, no. 6, pp. 3494–3500, 2004.

[10] K.-Y. Wong, W. Tang, K. M. Lau, and K. J. Chen, "Surface acoustic wave device on AlGaNGaN heterostructure using two-dimensional electron gas interdigital transducers," *Applied Physics Letters*, vol. 90, no. 21, p. 213506, 2007. [Online]. Available: http://ieeexplore.ieee.org/xpl/freeabs{_}all.jsp?arnumber=4827062{&}abstractAccess=no{&}userType=

[11] A. Mayorov, N. Hunter, W. Muchenje, C. Wood, M. Rosamond, E. Linfield, A. Davies, and J. Cunningham, "Surface acoustic wave generation and detection using graphene interdigitated transducers on lithium niobate," *Applied Physics Letters*, vol. 104, no. 8, p. 083509, 2014.

[12] M. Kurosawa, Y. Fukuda, M. Takasaki, and T. Higuchi, "A surface-acoustic-wave gyro sensor," *Sensors and Actuators A: Physical*, vol. 66, no. 1, pp. 33–39, 1998. [Online]. Available: http://www.sciencedirect.com/science/article/pii/S0924424797017135

[13] U. Wolff, F. L. Dickert, G. K. Fischerauer, W. Greibl, and C. C. Ruppel, "SAW sensors for harsh environments," *IEEE Sensors Journal*, vol. 1, no. 1, pp. 4–13, 2001.

[14] D. S. Stevens, J. C. Andle, S. Sabah, S. J. Jumani, B. W. Wall, M. Baier, T. Martens, and R. Gruenwald, "Applications of Wireless Temperature Measurement Using SAW Resonators," *Fourth International Symposium on Acoustic Wave Devices fo Future Mobile Communications Systems*, pp. 1–7, 2010. [Online]. Available: http://www.sengenuity.com/tech{_}ref/WIRELESS{_}TEMP{_}Applications.pdf

[15] W. E. Bulst, G. Fischerauer, and L. Reindl, "State of the Art in Wireless Sensing with Surface Acoustic Waves," *Industrial Electronics, IEEE Transactions on*, vol. 48, no. 2, pp. 265–271, 2001.

[16] A. Pohl, "A review of wireless SAW sensors," *IEEE Transactions on Ultrasonics, Ferroelectrics, and Frequency Control*, vol. 47, no. 2, pp. 317–332, 2000.

[17] H. Oh, K. J. Lee, K. Lee, and S. S. Yang, "Gyroscopes based on surface acoustic waves," *Micro and Nano Systems Letters*, vol. 3, no. 1, p. 1, Feb 2015. [Online]. Available: https://doi.org/10.1186/s40486-015-0009-z

[18] D. W.H.Hayd1, P.Hiesinger, R.S.Smith, B. and K. Summary, "Design of Quartz and Lithium Niobate Saw Resonators Using Aluminum Metallization."